

Microstructure and deformation in suspensions of soft microswimmers

Kiyoto Kubo¹ , Toshihiro Omori¹  and Takuji Ishikawa^{1,2} 

¹Department of Finemechanics, Tohoku University, Sendai 980-8579, Japan

²Department of Biomedical Engineering, Tohoku University, Sendai 980-8579, Japan

Corresponding author: Kiyoto Kubo, kiyoto.kubo.q5@dc.tohoku.ac.jp

(Received 18 July 2024; revised 17 November 2024; accepted 22 December 2024)

In recent years, various unique properties of microswimmer suspensions have been revealed. Some microswimmers are deformable; however, the influence of the swimmer's deformability has been overlooked. The present study examined the impact of soft microswimmers' membrane deformations in a mono-dispersed dense suspension on microstructure formation. Due to the small size of the microswimmers, the flow field is described by the Stokes equation. The soft microswimmer was modelled as a capsule with a two-dimensional hyperelastic membrane enclosing a Newtonian fluid that is driven by propulsion torques distributed slightly above the membrane surface. Changes to the torque distribution caused the soft swimmer to exhibit different swimming modes as a pusher or puller. Similar to rigid squirmers, soft swimmers displayed self-organised local clusters in the suspension. Membrane deformation changed the mutual interference among swimmers in the cluster, bringing the interactions closer together than those of rigid squirmers. Especially among soft pushers, rotational diffusion due to hydrodynamic interference was reduced and the swimming trajectory became relatively straight. As a result, polar order was less likely to form, especially in regions of high Ca . On the other hand, pullers showed strong interactions due to retraction flow and an increase in mean membrane tension. For pushers (pullers), the rear (side) interaction produced the greatest change in tension. These findings are expected to be useful for effort to understand the propulsion mechanisms of medical and industrial soft microrobots, as well as the biological responses of microorganisms induced by mechanical stimuli.

Key words: capsule/cell dynamics, collective behaviour, micro-organism dynamics

1. Introduction

Suspensions consisting of particles dispersed in a liquid are evident throughout nature and daily life; they are critical for industrial purposes in various fields and environments. Theoretical and experimental studies have been conducted in attempts to better understand and predict the rheological properties, microstructures and transport phenomena in such multiphase flows. In early theoretical studies, the analysis was limited to a dilute regime with a low Reynolds number. Where single- or two-particle interactions are dominant, the macroscopic suspension properties are commonly determined by the expansion of the volume fraction. For example, Einstein (1906) derived the effective viscosity of a dilute suspension of non-Brownian spheres, resulting in the first-order term of the viscosity as 2.5ϕ , where ϕ is the volume fraction. Batchelor (1970) derived a stress system of force-free particle suspensions by introducing the particle stress tensor, and Batchelor & Green (1972) calculated the bulk stress in the second-order term of the volume fraction from the two-body particle interactions. Particle deformability leads to deviation from the streamline during two-body interactions (Lac, Morel & Barthes-Biesel 2007). The shear-induced self-diffusion of droplets and red blood cells in the semi-dilute regime has been quantified from two-body hydrodynamic interactions (Loewenberg & Hinch 1997; Omori *et al.* 2013). The theory of dilute suspensions is well organised, and there are several relevant review articles (Brenner 1974; Jeffery & Acrivos 1976; Russel 1980; Davis & Acrivos 1985).

For suspensions with higher volume fractions, many-body interactions play a role. With respect to concentrated suspensions of rigid particles, it is necessary to accurately determine the lubrication forces acting between particles in near contact. Moreover, particle interactions at an infinite distance may be considered due to the long-range nature of Stokes flow. Stokesian dynamics that accurately compute both the short-range lubrication forces and long-range particle interactions has been developed and reviewed by Brady & Bossis (1988). For example, the shear-induced diffusion of Brownian particles in concentrated suspensions (Bossis & Brady 1987) and the rheological properties of concentrated suspensions of spheres (Brady & Bossis 1985) have been analysed using Stokesian dynamics. In a highly concentrated state, jamming phenomena can be observed at a critical volume fraction (≈ 0.64 for non-Brownian particles, Mari *et al.* (2014)), with the viscosity rapidly increasing when the volume fraction exceeds the critical threshold. Krieger & Dougherty (1959) derived an empirical equation of the viscosity from the dilute to the jamming regime. Blanc *et al.* (2013) reported the shear-induced anisotropic microstructure of non-Brownian particles in dense suspensions. Reviews about the rheology and microstructures of dense suspensions of rigid particles are presented in works by Ness, Seto & Mari (2022) and Guazzelli & Pouliquen (2018).

The suspension dynamics of microswimmers has received considerable interest in recent years, particularly in the fields of active fluids and active matter (Zöttl & Stark 2016; Saintillan 2018). The squirmer model, developed by Lighthill (1952) and Blake (1971), is widely used to describe the fluid dynamics of microswimmers (Ishikawa 2024). By varying the surface velocity distribution of the squirmer, it is possible to represent a range of velocity fields around the particle. This leads to various hydrodynamic interactions between the self-propelled particles, as reported in a number of interesting phenomena. Ishikawa, Simmonds & Pedley (2006) successfully introduced the squirmer model in analyses of the two-body interference problem. The model was extended to a Stokesian dynamics framework for concentrated monolayer suspensions (Ishikawa and Pedley 2008); they demonstrated that clustering and collective swimming of non-bottom-heavy strong pullers occurs, whereas for the weak puller and weak pusher,

a global coherent polar order was formed. Similar results have been demonstrated in the fully three-dimensional suspension (Ishikawa *et al.* 2008), where the global coherent structure of weak pullers was the result of short-range interactions between squirmers. The aggregation of pusher-type swimmers generates strong elongational flows, which may lead to instabilities in the particle structure (Ishikawa, Dang & Lauga 2022). Hydrodynamic interactions of ellipsoid squirmers were analysed using a boundary element method (Kyoya *et al.* 2015), and it was concluded that the nearest-neighbour two-body interference leads to collective swimming of the squirmers. The importance of the near-field interaction has also been reported by Yoshinaga & Liverpool (2008). After application of a lubrication force, a phase change is observed, whereby the gel-like cell aggregation transforms into a polar order with an aligned swimming direction. This is achieved by alteration of the swimming mode. The formation of a neutral-type coordinated swimming pattern is not observed in the absence of short-range interactions.

Some microswimmers are deformable, as evidenced by the behaviour of a ciliate in close proximity to a wall (Ishikawa & Kikuchi 2018). For example, the ciliate *Paramecium* exhibits a physiological response, termed the avoiding reaction, when its cell membrane is mechanically stimulated (Jennings 1904). The cell initially exhibits backward swimming motion, followed by rotational movement about its posterior end, before resuming normal forward locomotion. Membrane deformation and tension are important for understanding this microbial behaviour. Swimmer deformability may also influence short-range interactions. Menzel & Ohta (2012) developed a model of a soft self-propelled particle capable of deformation due to local pairwise interactions; they demonstrated that deformation could facilitate alignment effects between colliding particles, resulting in a rapid transition to a global ordered state with increasing deformability. A ring polymer model (Wen *et al.* 2022) and migrating cell model on a substrate (Coburn *et al.* 2013; Löber *et al.* 2015) have been proposed. These models showed that a swimmer's elastic behaviour alters migration and interparticle collisions, leading to changes in mean cluster diameter and degree of orientational order; notably, these models do not consider hydrodynamic interactions. Matsui, Omori & Ishikawa (2020a) analysed the impact of elastohydrodynamic interactions of capsule-type microswimmers using a boundary element–finite-element coupling method. The ciliary flow near the cell membrane was modelled as an external torque, in accordance with Ishikawa *et al.* (2016), utilising a two-dimensional hyperelastic constitutive law. Particle deformation reduces orbital displacement during two-body interference, suggesting that the self-diffusion of self-propelled particles could be suppressed by their deformability. Under shear flow, orientation in the vorticity direction has been observed (Matsui, Omori & Ishikawa 2020b), which was not observed for the rigid squirmer. Although these findings demonstrate the importance of particle deformation under hydrodynamic interaction, they are limited to the dilute regime. Thus, the impact of deformation in the dense regime including the effect of three or more body interferences remains unclear.

The objective of this study was to investigate the hydrodynamic interactions of soft microswimmers in a dense suspension. A hyperelastic capsule with a thrust torque was utilised as a soft swimmer (Matsui *et al.* 2020a,b). In this paper the basic equations and numerical method are presented in § 2. The effects of the membrane deformability and the swimming mode on the microstructure formation are investigated in § 3. The membrane tension induced by cell–cell interactions is discussed in § 4, and a summary of our findings and concluding remarks are presented in § 5.

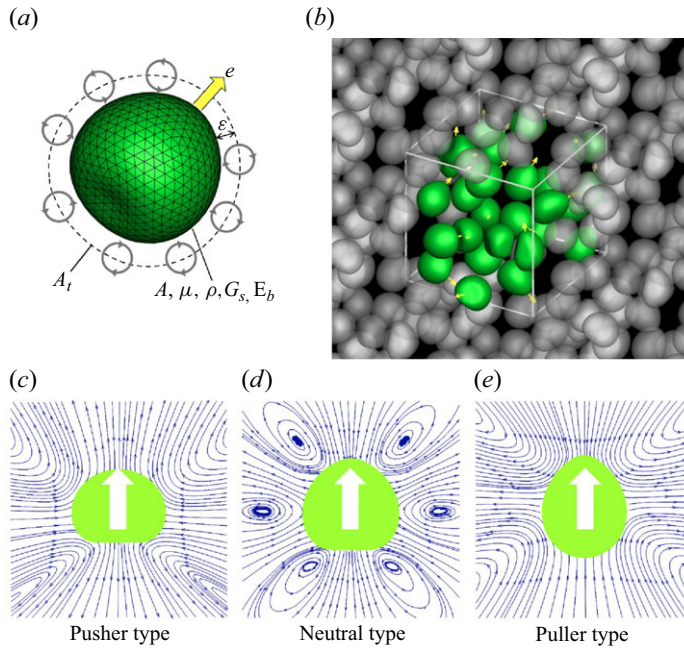


Figure 1. Problem settings and the soft microswimmer model. (a) Soft swimmer is modelled by a capsule with a hyperelastic thin membrane with the shear elastic modulus G_s and the bending modulus E_b . Propulsion torque is generated on the torque surface A_t (slightly above the membrane surface A). (b–d) Flow fields created by the soft swimmer. In this study, β is set to -0.9 for pushers, 0 for neutral swimmers and 0.9 for pullers. The white arrow indicates the swimming direction and blue arrow is the streamline. (e) Here 27 swimmers (depicted by green in the figure) are freely suspended in the computational unit and the triply periodic boundary condition is applied to the domain.

2. Basic equations and numerical methods

This section outlines the fundamental equations and the numerical model used in the present study. A torque-induced soft microswimmer developed by Ishikawa *et al.* (2016) was utilised. The methodology is briefly outlined here. For further details, please refer to Ishikawa *et al.* (2016) and Matsui *et al.* (2020a,b).

2.1. Soft microswimmer and problem settings

Consider microswimmers with a radius of a swimming freely in an incompressible Newtonian liquid with a viscosity of μ and a density of ρ . Due to the small size of the microswimmers, the particle Reynolds number is much smaller than unity, as such the inertial effect of the fluid flow can be neglected. The flow field is then governed by the Stokes equation. The microswimmer consists of a two-dimensional hyperelastic thin membrane enclosing a Newtonian liquid with the same viscosity and density as the external liquid. A torque swimmer model (Ishikawa *et al.* 2016) was originally developed to represent a ciliate. The model expresses the thrust force at the tip of a cilium and the reaction force at the root of the cilium as a torque on the surface A_t at a distance of ε from the membrane (cf. figure 1a). The magnitude of the propulsive torque density per unit area in the reference state L_r is given by

$$L_r = L_0 + \kappa \left(\theta - \frac{\pi}{2} \right), \quad (2.1)$$

where κ determines the torque strength of the asymmetry and θ is the polar angle with respect to the orientation vector \mathbf{e} .

The torque density L_0 is defined as the value at which the swimming speed of the rigid body is equal to U_0 . The swimmer in the reference state satisfies the torque-free condition on the overall torque surface due to the axisymmetric torque distribution. The instantaneous torque density per unit area in the deformed state L is given by

$$L = L_r \frac{dA_{t,r}}{dA_t}, \quad (2.2)$$

where $dA_{t,r}$ and dA_t are the local torque surface area in the reference and deformed states, respectively. This correction means that the number of cilia does not change with deformation. The propulsive torque in vector form is given by $\mathbf{L} = L\mathbf{n} \times \mathbf{t}$, where \mathbf{n} is the unit outward normal vector and \mathbf{t} is the unit tangential vector in the θ direction on the membrane surface. The soft swimmer is deformed from its reference shape by the propulsive torque distribution, resulting in a swimming-induced stresslet \mathbf{S} (Matsui *et al.* 2020b):

$$\mathbf{S} = \int \left[\frac{1}{2}(\mathbf{q}\mathbf{x} + \mathbf{x}\mathbf{q}) - \frac{1}{3}\mathbf{q} \cdot \mathbf{x}\mathbf{I} \right] dA, \quad (2.3)$$

where \mathbf{q} is the traction at the point \mathbf{x} on the membrane A and \mathbf{I} is the identity matrix. By changing κ in (2.1), various swimming modes can be expressed as puller, neutral and pusher types (figure 1b–d), respectively. In the rigid squirmer (Blake 1971), the swimming mode is often expressed by positive and negative values of the second mode β :

$$v_\theta = U_0 \left(\frac{3}{2} \sin \theta + \frac{3}{2} \beta \sin \theta \cos \theta \right). \quad (2.4)$$

Here v_θ is the squirming velocity on the squirmer surface. In this study the swimming mode is also defined using β obtained from \mathbf{S} with reference to the rigid squirmer model, i.e.

$$S_{ee} = 4\pi\mu a^2\beta, \quad (2.5)$$

where S_{ee} is the stresslet component in the swimming direction. Here κ is adjusted to ensure that, under the same β , the stresslet produced by the rigid squirmer and the soft swimmer are the same. The correspondences between κ and β are almost linear as shown in figure 2. In this study, β is set to -0.9 for pushers, 0 for neutral swimmers and 0.9 for pullers.

Assuming an infinite suspension, triply periodic boundary conditions were applied, as shown in figure 1(e). Twenty-seven soft swimmers with random orientations were placed in random initial positions in the computational unit domain. The volume fraction ϕ was varied from 0.03 to 0.2 by changing the domain size. According to the scaling by Batchelor & Green (1972), the frequency of n -body interference is proportional to ϕ^n . Thus, for $\phi = 0.2$, the influence of three-body interference is expected to be 20% of two-body interference.

2.2. Membrane mechanics

The coupling of thin-shell theory of capsules with fluid mechanics has been developed by the work of Barthès-Biesel, Pozrikidis and their co-workers. Therefore, we briefly explain the outline of thin-shell theory in the main text. For further details, please refer to Barthès-Biesel *et al.* (2002), Lac *et al.* (2004), Walter *et al.* (2010) and Pozrikidis (2010). The swimmer's membrane is modelled as a hyperelastic thin material. A material point of

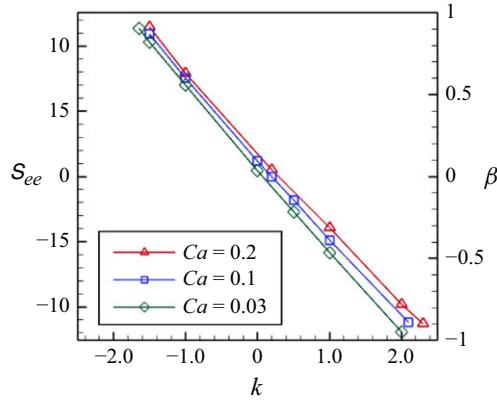


Figure 2. The relationship between the asymmetry of torque strength κ , the stresslet component in the swimming direction S_{ee} and the swimming mode β of the soft swimmer with each Ca . Here Ca is the ratio between the viscous force due to swimming and the elastic force of the membrane defined by (2.22).

the membrane in the reference state is represented by \mathbf{X} ; $\mathbf{x}(\mathbf{X}, t)$ expresses the deformed state. Using a surface deformation gradient tensor \mathbf{F}_s , reference and deformed states have the following relationship (Pozrikidis 2010):

$$d\mathbf{x} = \mathbf{F}_s \cdot d\mathbf{X}, \quad (2.6)$$

where $\mathbf{F}_s = \partial \mathbf{x} / \partial \mathbf{X}$. The Green–Lagrange strain tensor \mathbf{E} describing local deformation of the membrane is as follows:

$$\mathbf{E} = \frac{1}{2} (\mathbf{F}_s^T \mathbf{F}_s - \mathbf{I}). \quad (2.7)$$

The first and second invariants of the strain tensor are given by the principal extension ratios λ_1 and λ_2 as

$$I_1 = \lambda_1^2 + \lambda_2^2 - 2 \quad (2.8)$$

and

$$I_2 = \lambda_1^2 \lambda_2^2 - 1 = J_s^2 - 1, \quad (2.9)$$

where $J_s = \det(\mathbf{F}_s) = \lambda_1 \lambda_2$ is the Jacobian expressing the area dilatation. Because the membrane is modelled as a two-dimensional hyperelastic material, the Cauchy tension \mathbf{T}_s and the strain energy function $w_s(I_1, I_2)$ have the following relationship:

$$\mathbf{T}_s = \frac{1}{J_s} \mathbf{F}_s \cdot \frac{\partial w_s}{\partial \mathbf{E}} \cdot \mathbf{F}_s^T. \quad (2.10)$$

In order to express strain hardening behaviour and the incompressible areal dilatation of a biological membrane, we utilise the constitutive law proposed by Skalak *et al.* (1973). The strain energy function of the Skalak model is given by

$$w_s = \frac{G_s}{4} (I_1^2 + 2I_1 - 2I_2 + CI_2^2), \quad (2.11)$$

where G_s is the surface shear elastic modulus and C is the non-dimensional areal dilatation constant. The Poisson ratio of the Skalak law is $\nu_s = C/(1 + C)$. The value of C is set to 10 with reference to the erythrocyte model (Omori *et al.* 2013).

The bending energy of the biological membrane, derived by Helfrich (1973), is

$$w_b = \frac{E_b}{2} \int (2H - c_0) dA, \quad (2.12)$$

where H is the mean curvature of the membrane, c_0 is the spontaneous curvature and E_b is the bending modulus. By assuming a symmetric membrane property (i.e. $c_0 = 0$), the energy can be converted to the force density \mathbf{q}_b as (Matsui *et al.* 2020a)

$$\mathbf{q}_b = -2E_b[\Delta_s H + 2H(H^2 - K)]\mathbf{n}, \quad (2.13)$$

where Δ_s is the Laplace–Beltrami operator and K is the Gaussian curvature on the membrane surface.

2.3. Fluid mechanics

Due to the small size of the swimmer, the inertial effect of fluid flow is negligible. Therefore, the flow field is governed by the Stokes equation, and the fluid velocity \mathbf{v} at an arbitrary point \mathbf{y} is given by the boundary integral equation (Pozrikidis 1992) as

$$\mathbf{v}(\mathbf{y}) = -\frac{1}{8\pi\mu} \sum_i^N \left[\int_A \mathbf{J}(\mathbf{x}, \mathbf{y}) \cdot \mathbf{q}(\mathbf{x}) dA^i + \int_{A_t} \mathbf{R}(\mathbf{x}, \mathbf{y}) \cdot \mathbf{L}(\mathbf{x}) dA_t^i \right], \quad (2.14)$$

where N is the number of microswimmers in the fluid domain. Here, \mathbf{J} and \mathbf{R} are the Green's function of the Stokeslet and torque in the triply periodic boundaries, respectively (Beenakker 1986):

$$\mathbf{J} = \mathbf{J}^1 + \mathbf{J}^2, \quad (2.15)$$

$$\mathbf{R} = \mathbf{R}^1 + \mathbf{R}^2, \quad (2.16)$$

$$\begin{bmatrix} J_{ij}^1 \\ J_{ij}^2 \end{bmatrix} = (\delta_{ij} \nabla^2 - \nabla_i \nabla_j) \begin{bmatrix} r \operatorname{erfc}(\xi r) \\ r \operatorname{erf}(\xi r) \end{bmatrix}, \quad (2.17)$$

$$\begin{bmatrix} R_{ij}^1 \\ R_{ij}^2 \end{bmatrix} = \frac{1}{4} \varepsilon_{lkj} (\nabla_k - \nabla_l) \begin{bmatrix} J_{il}^1 \\ J_{ik}^2 \end{bmatrix}, \quad (2.18)$$

where δ is the Kronecker delta, ε is the Levi-Civita epsilon and ξ is an arbitrary positive constant with dimensions of inverse length for controlling the convergence rate of the error function and complementary error function. For a simple cubic lattice, the optimal value of the convergence rate that minimises the computational cost for the periodic expansion is given by $\sqrt{\pi}/V^{1/3}$ (Pozrikidis 1992), where V is the volume of the computational domain. The traction \mathbf{q} is given by the stress jump across the thin membrane as

$$\mathbf{q}(\mathbf{x}) = [\boldsymbol{\sigma}_{out}(\mathbf{x}) - \boldsymbol{\sigma}_{in}(\mathbf{x})] \cdot \mathbf{n}(\mathbf{x}), \quad (2.19)$$

where $\boldsymbol{\sigma}_{in}$ and $\boldsymbol{\sigma}_{out}$ represent viscous stress on the surface from inside and outside of the membrane, respectively.

2.4. Numerical methods

In this section we briefly explain the numerical method. The swimmer's membrane and torque surface are respectively discretised by 1280 triangular elements, with 642 vertices, as shown in figure 1(a). Each material point is tracked in terms of its associated Lagrangian, and the strain at any time t is determined. The tension is calculated based

on Skalak's constitutive law, and the load \mathbf{q} acting on the membrane is obtained from the weak-form equilibrium equation, given as

$$\int_A \hat{\mathbf{u}} \cdot \mathbf{q}_s dA = \int_A \hat{\boldsymbol{\varepsilon}} : \mathbf{T}_s dA, \quad (2.20)$$

where $\hat{\mathbf{u}}$ is the virtual displacement and $\hat{\boldsymbol{\varepsilon}} = (1/2)(\nabla_s \hat{\mathbf{u}} + \nabla_s \hat{\mathbf{u}}^T)$ is the virtual strain. The above equation is solved using a finite-element method (Walter *et al.* 2010) with respect to unknown \mathbf{q}_s . Assuming a linear sum of the loads due to in-plane deformation and the loads due to bending deformation, the load on the membrane surface is determined by $\mathbf{q} = \mathbf{q}_s + \mathbf{q}_b$. When \mathbf{q} is obtained, it is substituted into the boundary integral equation; the velocity \mathbf{v} is computed using a Gaussian quadrature method with six numerical integration points in each element. A material point on the torque surface \mathbf{x}_t is given by $\mathbf{x}_t = \mathbf{x} + \varepsilon \mathbf{n}(\mathbf{x})$, and the flow due to the torque \mathbf{L} is calculated in the same manner. In order to coincide with the half-length of the cilia, ε is set to $0.05a$, where a is the radius of the swimmer. Assuming a no-slip boundary at the membrane, $d\mathbf{x}/dt = \mathbf{v}$, the material point \mathbf{x} is updated by a second-order Runge–Kutta method. The above cycles are iteratively calculated to simulate hydrodynamic interactions in the suspension.

A multiple expansion technique is introduced to accelerate the computation (Pozrikidis 1992). Depending on the distance between swimmers' centres, three regions corresponding to (i) short-range, (ii) middle-range and (iii) long-range interactions are considered in the calculation. For the short-range interaction ($r \leq r_{sm}$), the boundary integral equations are numerically integrated using all 1280 elements. In the middle-range interaction ($r_{sm} < r \leq r_{ml}$), a coarse-grained 20 triangle mesh is used for the calculation; the point stresslet and torque defined at each mass centre are utilised for long-range interactions ($r > r_{ml}$). Threshold values $r_{sm} = 4a$ and $r_{ml} = V^{1/3}$ were set to preserve computational accuracy.

The overlap between meshes becomes problematic when the swimmers are very close together (i.e. of the order of the mesh size). Assuming repulsion between cilia, the repulsive force at very short distances is defined as

$$\mathbf{F}_{rep}(\mathbf{r}') = \begin{cases} k(2.4\varepsilon - |\mathbf{r}'|) \frac{\mathbf{r}'}{|\mathbf{r}'|} & (|\mathbf{r}'| \leq 2.4\varepsilon), \\ \mathbf{0} & (|\mathbf{r}'| > 2.4\varepsilon), \end{cases} \quad (2.21)$$

where \mathbf{r}' is the distance between node points on the torque surface of each swimmer and k represents the magnitude of the repulsion. In this study, $k/\mu U_0 = 500$ was set to be consistent with the ciliary elasticity estimated from the bending stiffness of the cilia (Katoh *et al.* 2023).

Membrane deformability is normalised by the capillary number Ca :

$$Ca = \frac{\mu U_0}{G_s}. \quad (2.22)$$

This dimensionless number represents the ratio between the viscous force due to swimming and the elastic force of the membrane. All computations were normalised by using the radius a , swimming speed U_0 and surface shear elastic modulus G_s . Here ϕ was changed by varying the length, whereas the number of swimmers remained fixed at 27.

3. Microstructure

We first show hydrodynamic interactions of puller-type swimmers in figure 3. Swimmers were initially assigned random positions and orientations. Here ϕ was set to 0.1 and the

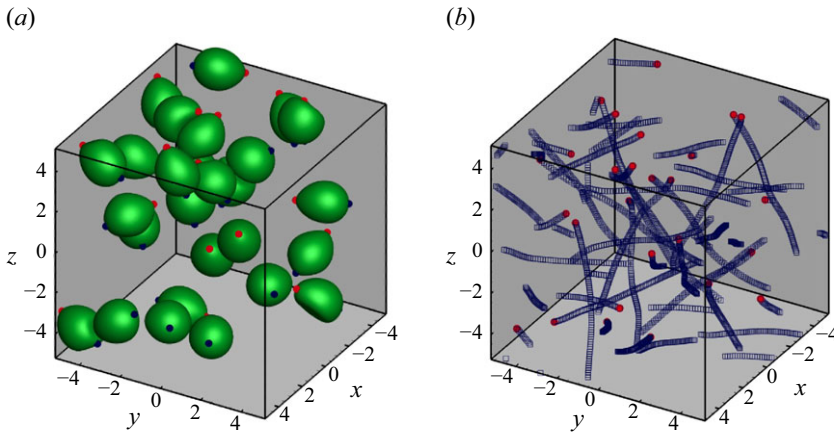


Figure 3. Puller swimmers with $Ca = 0.1$ and $\phi = 0.1$. (a) Instantaneous snapshot of 27 pullers. Red and blue markers indicate the head and tail points, respectively. (b) Trajectories of 27 swimmers. Red markers indicate each final position of the mass centres.

capillary number was $Ca = 0.1$. In the suspension the pullers repeatedly interacted with large deformations, forming small clusters. The trajectories slightly changed during the interaction, as shown in figure 3(b). When the pullers passed each other, they swam in relatively straight lines.

3.1. Orientational correlations

For a more quantitative analysis, we define self-correlation of the swimming direction from the initial direction as

$$I_{e_0}(t) = \langle \mathbf{e}_i(t) \cdot \mathbf{e}_i(0) \rangle_N, \quad (3.1)$$

where the bracket $\langle \rangle_N$ represents an ensemble average over the number of swimmers N , \mathbf{e}_i is the orientation vector of the i th swimmer defined from the posterior and anterior node points. The result is shown in figure 4(c), in which the correlation gradually decreases over time. The relaxation time, corresponding to the time when $I_{e_0} = 1/e$ (e is Napier's constant), was approximately estimated in the range of $100 \leq tU_0/a \leq 200$ for $Ca = 0.03, 0.1$ and 0.2 , whereas that of the rigid puller (Ishikawa & Pedley 2007) was approximately $tU_0/a \simeq 50$. With respect to soft swimmers, the scattering angles after face-to-face interaction are reduced according to deformability (Matsui *et al.* 2020a). Thus, the self-correlation to the initial swimming direction persists for a longer duration as Ca increases, and the swimmers retain their initial orientations longer compared with rigid swimmers. We also investigated the self-correlation of pusher and neutral swimmers (cf. figures 4a and 4b). Pusher and neutral soft swimmers tend to have longer relaxation times relative to rigid squirmers, as do pullers.

In order to investigate the time scale for microstructure development in the suspension, the global order correlation is defined as

$$I_e(t) = \langle \mathbf{e}_i(t) \cdot \mathbf{e}_j(t) \rangle_N. \quad (3.2)$$

To ensure that they would not affect the final structure, two initial conditions were set: (i) an initial polar order and (ii) an initial random configuration. The global correlation of the swimming directions reached a developed state when $tU_0/a > 100$ for pushers (cf. figure 5a) and $tU_0/a > 200$ for pullers (cf. figure 5b). These times were close to

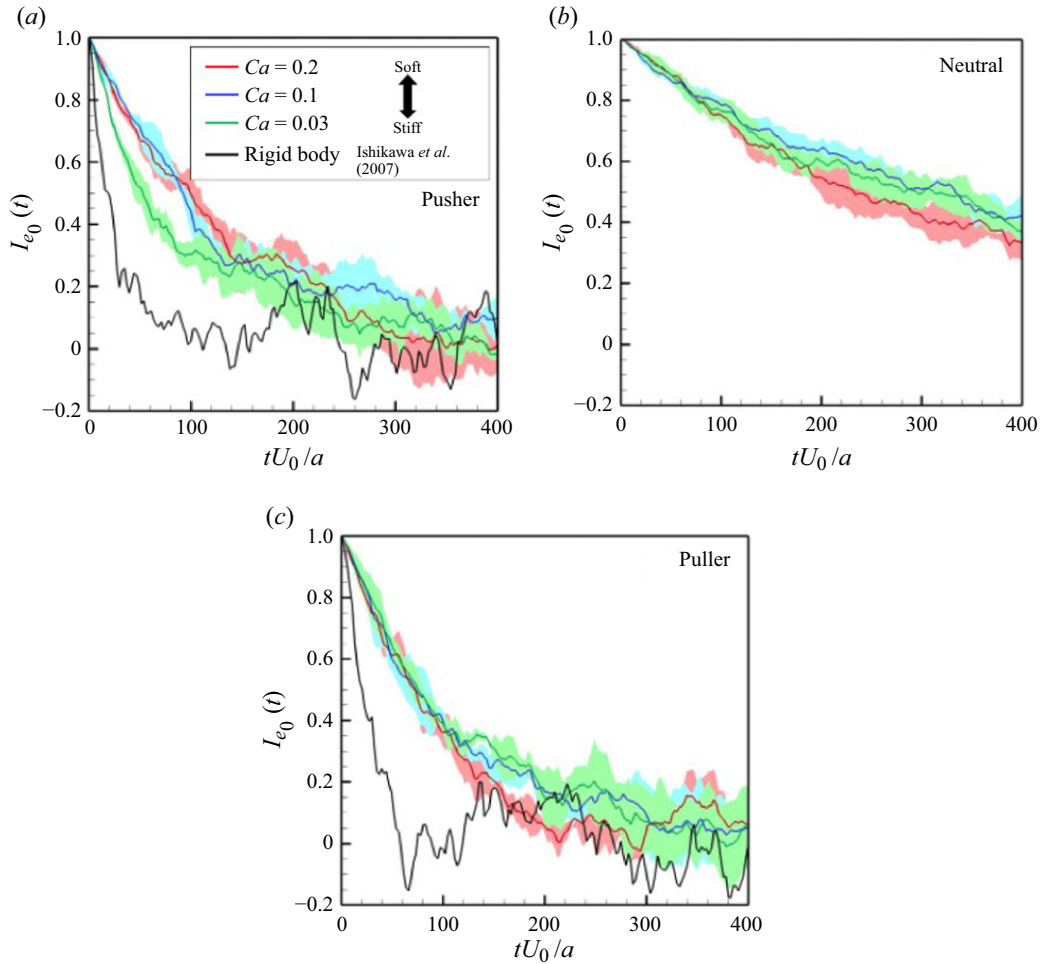


Figure 4. Self-correlations of swimmers' orientations $I_{e_0}(t) (= \langle \mathbf{e}_i(t) \cdot \mathbf{e}_i(0) \rangle)$ in the suspension with $\phi = 0.1$. Here \mathbf{e}_i is the swimming direction of the i th swimmer. The coloured lines and area shows the averaged values and standard deviations for the three independent cases throughout the paper. The black lines show the result of rigid squirmers reported by Ishikawa & Pedley (2007).

the relaxation times of the self-correlation; the converged values of I_e were almost 0 for pushers and 0.2 for pullers. These results suggest that pullers achieve collective swimming, in which the swimmers are more aligned with each other's swimming direction relative to pushers, similar to the behaviour of rigid squirmers (Ishikawa & Pedley 2007).

We then investigated the spatial correlations of the swimmers in the developed state. Based on the results in figure 5, the criterion for determining a sufficiently developed microstructure was set to $tU_0/a = 200$, and the spatial correlation considered the time average between $tU_0/a = 200$ and 400. For neutral swimmers, structural development was very slow and convergence values could not be obtained beyond $tU_0/a = 1000$. Thus, in the following sections we focus on the comparison between pushers and pullers; the results for neutral swimmers can be found in the Appendix. The spatial correlation function of the swimmers' orientations within the radial interval $r_g - \Delta r$ to r_g is defined as

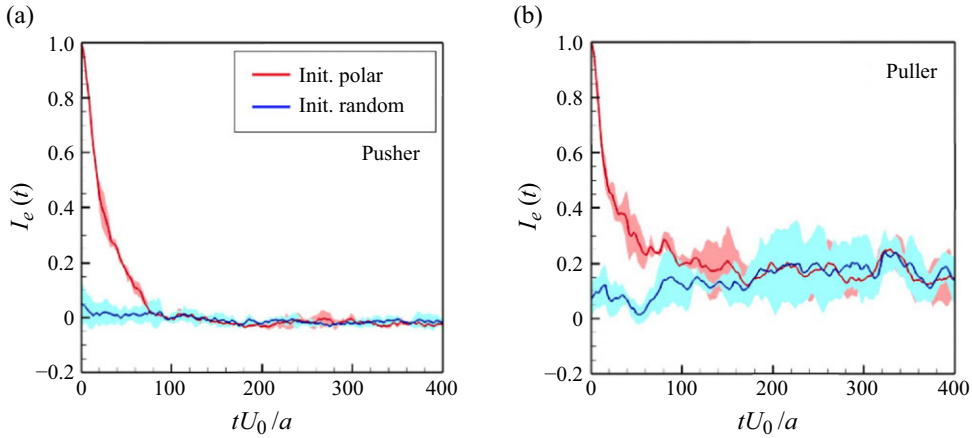


Figure 5. Time change of the global correlation of swimmers' orientations $I_e(t) (= \langle \mathbf{e}_i(t) \cdot \mathbf{e}_j(t) \rangle)$ with $\phi = 0.1$ and $Ca = 0.1$.

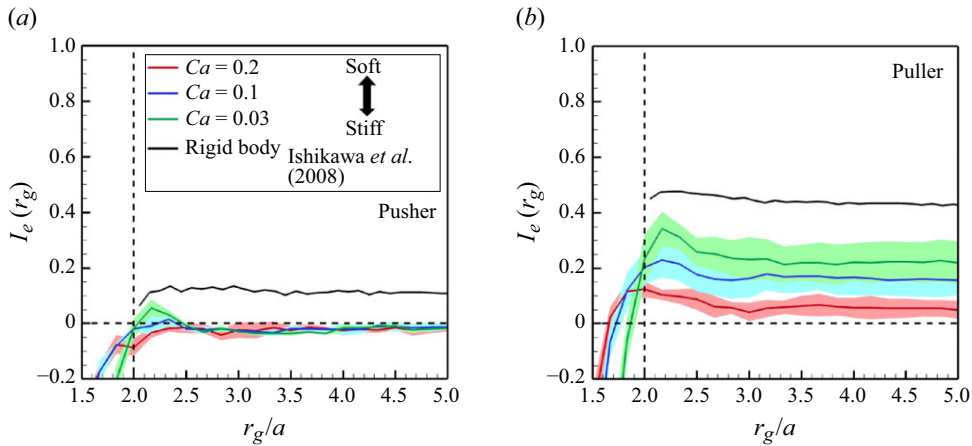


Figure 6. Correlations of swimmers' orientations as a function of relative distance $I_e(r_g) (= \langle \mathbf{e}_i(r_i) \cdot \mathbf{e}_j(r_j) \rangle)$ with the $\phi = 0.1$ in the developed state. The black lines show the result of rigid squirmers.

$$I_e(r_g) = \langle \mathbf{e}_i(\mathbf{r}_i) \cdot \mathbf{e}_j(\mathbf{r}_j) \rangle_{N,t}, \quad (3.3)$$

where r_g is the relative centre–centre distance of the swimmers, \mathbf{r}_i is the mass centre of the i th swimmer and the mass centre of the j th swimmer within the interval is given by $\mathbf{r}_j \in (r_g - \Delta r) \leq |\mathbf{r}_j - \mathbf{r}_i| \leq r_g$. In this study, Δr is defined as a constant that divides the domain length into 60 sampling points. The results are shown in figure 6. For the comparison, the results of rigid squirmers (Ishikawa *et al.* 2008) are also presented. Ishikawa *et al.* (2008) simulated three-dimensional suspensions with 64 rigid squirmers applied with periodic boundary conditions and then reported that hydrodynamic interactions form long-ranged orientational correlations of the domain size level ($r_g/a \approx 7$). Negatively correlated interactions were not observed among rigid swimmers, whereas high Ca swimmers showed negative correlations. Negative areas extended to the long range, especially among pushers. The correlations of soft swimmers maintain up to the domain size level, similar to the rigid swimmers. Since it is difficult to increase the domain size further due to computational constraints, innovations in computers and computational

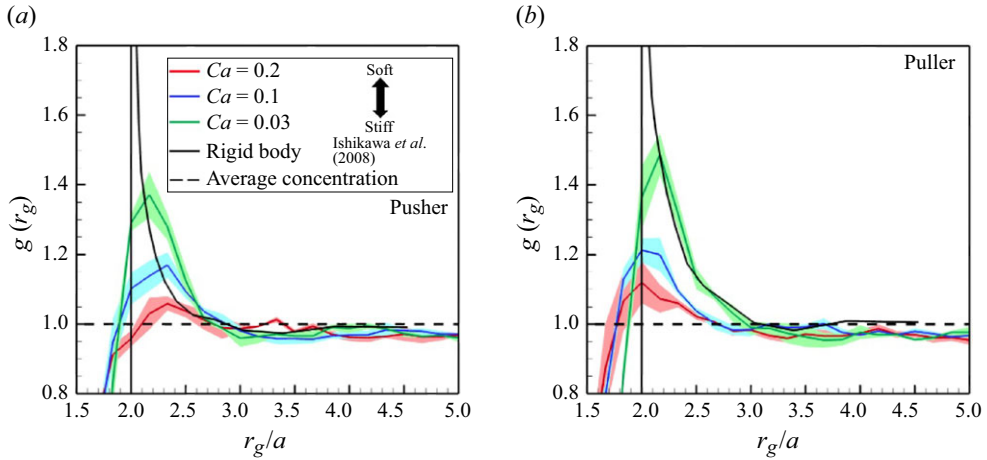


Figure 7. Swimmers' aggregations in the suspension with $\phi = 0.1$. The black broken line indicates $g = 1.0$, where the local number density is equivalent to the global number density. The black solid lines show the result of rigid squirmers (Ishikawa *et al.* 2008).

methods are needed to discuss larger scales. These results suggest that deformability enables swimmers to easily pass each other (e.g. during face-to-face interactions). The effects of membrane deformation are therefore expected to weaken the swimming-induced microstructure formation.

3.2. Swimmer aggregation

In order to quantify swimmer aggregation, the radial distribution function $g(r_g)$ is introduced as

$$g(r_g) = \frac{\langle n(r_g) \rangle_{N,t}}{n_{mean}}, \quad (3.4)$$

where $n_{mean} = N/V$ is the global mean of the number density. The local number density $n(r_g)$ is defined by the number of swimmers within the spherical shell domain of radius $r_g - \Delta r$ to r_g .

The aggregation ratio g of pushers and pullers is shown in figure 7. Both pushers and pullers tended to aggregate within $r_g \approx 3a$ in all cases, a tendency similar to the rigid squirmers (Ishikawa *et al.* 2008). However, due to the membrane deformability, soft swimmers aggregated closer than $r_g = 2a$, which is equivalent to the contact distance of rigid swimmers. Higher capillary numbers allowed swimmers to aggregate more closely, but the peak value of g was considerably reduced. Concerning rigid swimmers, the values were high very close to swimmers with $r_g \simeq 2a$ and converged to an average value of 1 at a distance of $r_g \geq 3a$. The number of swimmers forming a cluster is estimated by integrating $\langle n(r_g) \rangle$ in the region where the swimmer density is greater than the mean. The results are summarised in table 1; in all cases, the clusters were formed by approximately two to three swimmers.

3.3. Swimming speed

The ensemble average of the swimming speed $\langle |U_i| \rangle_N(t)$ was computed from $200 \leq tU_0/a \leq 400$. The time-averaged value is represented by $\langle \bar{U} \rangle$. Figure 8 shows $\langle \bar{U} \rangle$

Ca	Pusher type	Pusher type
0.2	1.89	2.53
0.1	2.39	2.03
0.03	1.98	2.51
Rigid*	2.49	2.63

Table 1. Average number of swimmers in a unit cluster. The marker ‘*’ shows reference to the previous results of rigid squirmer models provided by Ishikawa *et al.* (2008).

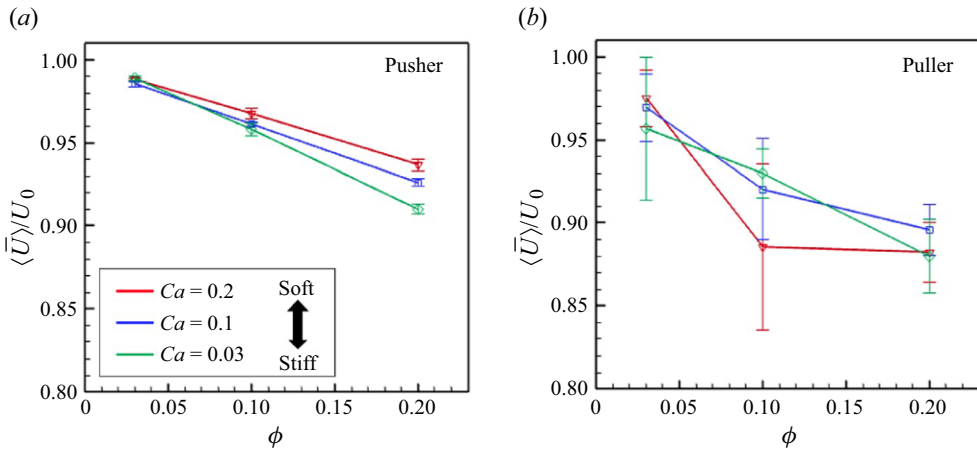


Figure 8. Time-averaged swimming speeds of the swimmers with various Ca . The error bar indicates the standard deviations computed from independent three initial conditions.

as a function of ϕ , with $Ca = 0.03, 0.1$ and 0.2 . For both pushers and pullers, $\langle \bar{U} \rangle$ monotonically decreased according to ϕ . For the same number density and Ca , the average swimming speed of pushers exceeded that of pullers. This is because pushers can more easily pass each other. Among pusher swimmers, a higher Ca value leads to faster swimming under the same number density conditions.

Translational dispersion is a measure of microswimmer spreading. The mean square displacement R^2 was used to determine the swimmer's self-dispersion, as given by

$$R^2(\Delta t) = \langle |\mathbf{r}_i(t + \Delta t) - \mathbf{r}_i(t)|^2 \rangle_N, \quad (3.5)$$

where \mathbf{r} is the swimmer's displacement, Δt is the time interval and R^2 is a function of Δt with $\phi = 0.20$, as shown in figure 9. We observed the different effects of Ca between pushers and pullers. Among pushers, the value was higher for larger Ca in the high Δt regime, whereas it was almost invariant for Ca among pullers. In the double logarithmic axes (cf. inset graph in figure 9), both pushers and pullers had a slope of 2. Thus, the swimmers' movement was ballistic, rather than diffusive, in the range of $\Delta t U_0/a \leq 100$. A longer Δt analysis may ultimately lead to a transition to diffusion; however, the computational time interval $\Delta t U_0/a \leq 100$ is not sufficient to confirm this transition. Since the time scale of the relaxation time for orientational self-correlation is estimated as $O(10^2)$, a time scale of $O(10^3)$ may be required to observe a diffusion phenomenon, which is difficult to achieve due to the long computational time. The converged values could not be confirmed in this study.

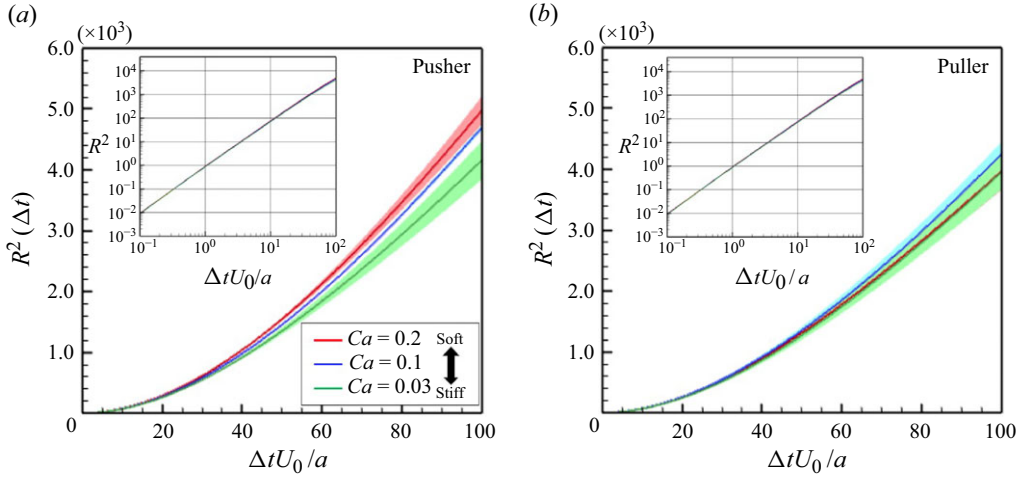


Figure 9. Mean square displacements R^2 in the suspension with $\phi = 0.2$ during the time interval Δt . The inserted graph is drawn to a double logarithmic scale.

3.4. Rotational diffusivity

Rotational diffusivity D_R is defined as follows to describe scattering in the swimming direction:

$$D_R(\Delta t) = \lim_{\Delta t \rightarrow \infty} \frac{\langle (\boldsymbol{\omega}(t + \Delta t) - \boldsymbol{\omega}(t)) \otimes (\boldsymbol{\omega}(t + \Delta t) - \boldsymbol{\omega}(t)) \rangle_N}{2\Delta t}, \quad (3.6)$$

$$\boldsymbol{\omega}(t + \Delta t) - \boldsymbol{\omega}(t) = \int_t^{t+\Delta t} \boldsymbol{\Omega} dt. \quad (3.7)$$

Here $\boldsymbol{\Omega}$ is the swimmer's rotational velocity and $\boldsymbol{\omega}$ is the rotational displacement. The average of the diagonal components of D_R represents the isotropic contribution:

$$D_R = (D_{R,xx} + D_{R,yy} + D_{R,zz})/3. \quad (3.8)$$

The time change of D_R with $\phi = 0.10$ and 0.20 is shown in figure 10. Here D_R linearly increases in the small Δt regime ($\Delta t U_0/a < 1$) and then gradually converges to a specific value at $\Delta t U_0/a \geq 10$. This tendency is similar to that of rigid swimmers (Ishikawa & Pedley 2007). Regarding soft pushers, the converged value was slightly smaller with increasing Ca , which suggests that softer pushers can maintain their swimming direction during the interaction, (i.e. the softer pusher has highly direct swimmability). Among pullers, D_R was slightly higher with Ca . In addition, we observed long and stable two-body clusters during face-to-face collisions, and D_R convergence became worse (cf. figure 10 b).

To further analyse the short-range interactions, the effects of swimming mode on the nearby swimmer distribution were examined. Because most clusters were formed by two or three swimmers (cf. table 1), we focused on the closest two-body interaction. The distributions of the closest swimmers during the short-range interaction were quantified, and the probability density P was derived as a function of α . Here α is the relative angle between the closest swimmers i and j , (i.e. the angle in which the closest swimmer j is from the direction of \mathbf{e}_i):

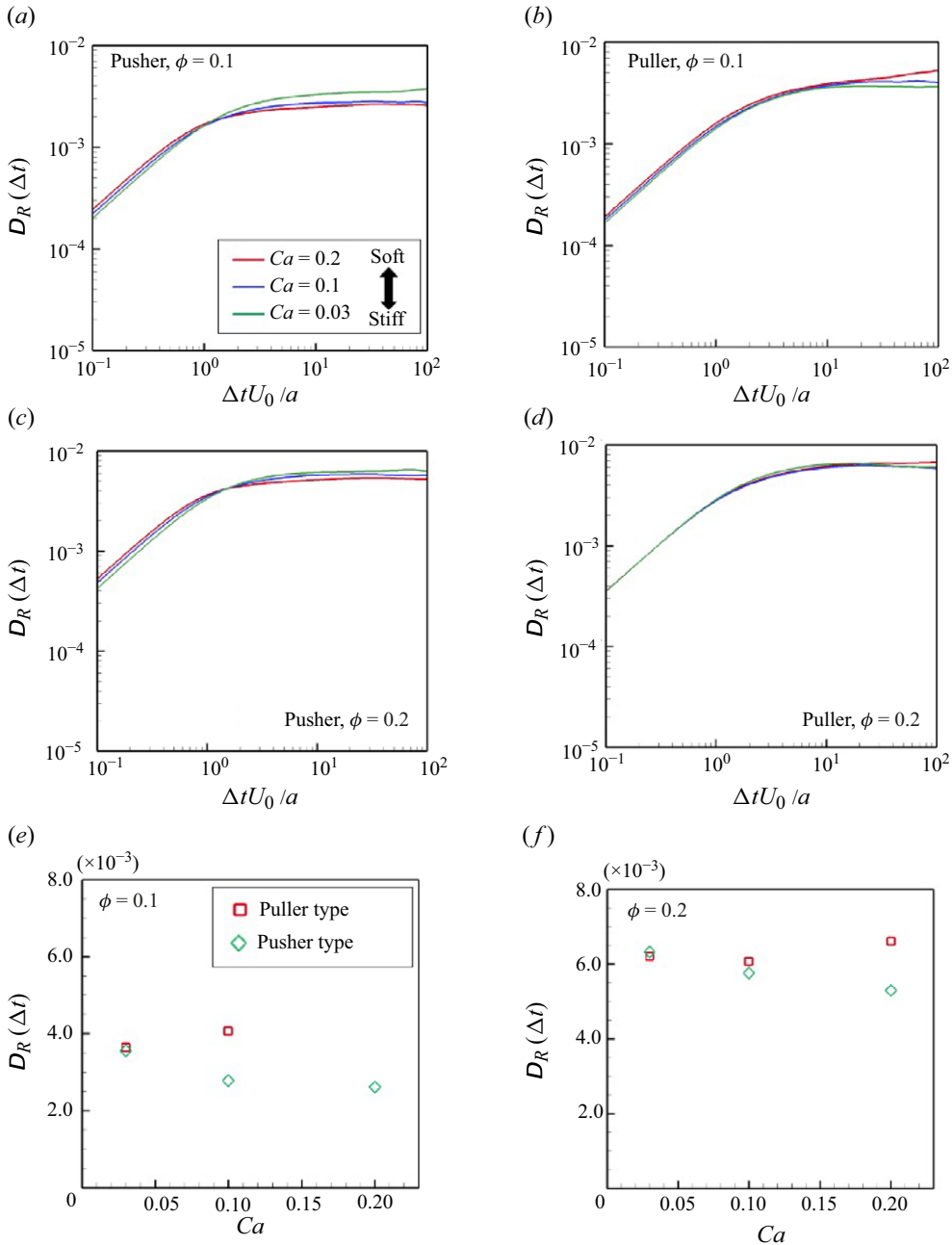


Figure 10. (a–d) Time change of swimmers' rotational diffusivities during the time interval Δt ; (a,b) $\phi = 0.1$ and (c,d) $\phi = 0.2$. Converged values of D_R in the suspension with (e) $\phi = 0.1$ and (f) $\phi = 0.2$. (Note that the result of the puller type with $Ca = 0.2$ is excluded because the convergent value has not been obtained during the time scale that has been simulated.)

$$\alpha = \cos^{-1} \left(\frac{\mathbf{e}_i \cdot (\mathbf{r}_j - \mathbf{r}_i)}{|\mathbf{r}_j - \mathbf{r}_i|} \right). \quad (3.9)$$

As shown in figure 11, pushers with low Ca exhibited asymmetric distributions of $P(\alpha)$, and the peak appeared in the range of $\pi/3 < \alpha < \pi/2$. As Ca increases, the peak shifted

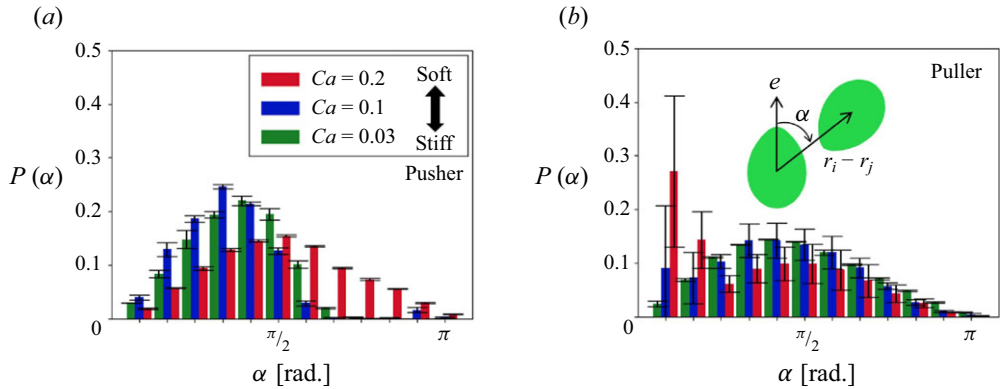


Figure 11. Probability density of the nearest neighbours as a function of relative angle α from the swimming direction ($\phi = 0.1$).

to $\pi/2$ and the distribution became almost symmetric. With respect to pullers with high Ca , a large peak was observed at $\alpha < \pi/12$, indicating that a soft puller is likely to collide with the head. Among pullers, structures with heads coalesced due to the retracted flow have also been reported for the ellipsoidal squirmers (Kyoya *et al.* 2015); the results of the present study are consistent with this finding.

4. Deformation and tension

Membrane tension is important for the analysis of capsule dynamics in a suspension (Walter *et al.* 2011; Omori *et al.* 2012). For example, Walter *et al.* (2011) reported that membrane wrinkling and buckling occurs due to local compression in the low Ca regime, whereas the capsule is extremely elongated at the tip in the high Ca regime. Membrane tension is also associated with mechanosensing mechanisms in swimming microorganisms (Matsui *et al.* 2020a). How does the cellular microstructure presented in the previous section relate to the membrane tension of the microswimmer? In this section we investigate the deformation and membrane tension of the microswimmer during many-body hydrodynamic interactions.

4.1. Strain

In order to quantify membrane deformation, we utilised the second invariant of the strain tensor I_2 within the short-range interaction ($r < 3a$). The second invariant represents the area dilatation of the membrane, which controls the mechanosensitive channel of prokaryotes during severe osmotic challenges (Sukharev *et al.* 1997; Perozo *et al.* 2002). The time- and ensemble-averaged strain increment ΔI_2 relative to the solitary swimming is presented in figure 12. As indicated in figure 12(a), ΔI_2 was nearly proportional to Ca for both pushers and pullers. This phenomenon represents a direct consequence of an increase in Ca , resulting in reduced membrane rigidity. Here ΔI_2 was greater for pullers than for pushers, due to the pulling effect in the swimming direction. We also investigated the effect of the volume fraction ϕ on deformation (cf. figure 12b). A linear trend was observed for the volume fraction. A greater volume fraction led to more frequent microswimmer collisions, resulting in larger deformation.

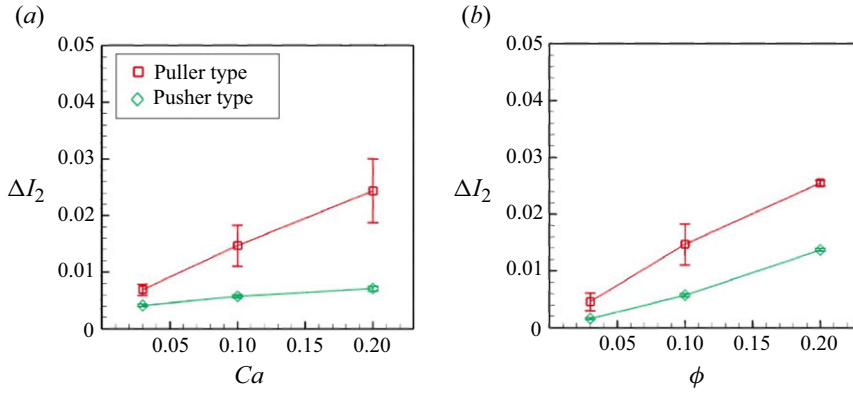


Figure 12. Difference of the second strain invariant from the solitary swimming: (a) effect of Ca ($\phi = 0.1$) and (b) effect of ϕ ($Ca = 0.1$).

4.2. Tension

We evaluated the principal tension during the interaction. The principal tension τ_1 of the Skalak law is given by

$$\tau_1 = \frac{G_s \lambda_1}{\lambda_2} (\lambda_1^2 - 1 + C \lambda_2^2 I_2) \quad (4.1)$$

and τ_2 is obtained by switching λ_1 and λ_2 . Because the in-plane isotropic tension T , defined as $T = (\tau_1 + \tau_2)/2$, could be relevant for activation of the mechanosensing ion channel (Matsui *et al.* 2020a), we focused on the in-plane isotropic tension T .

In this study the reference shape of the elastic membrane was assumed to be a sphere. Membrane tension was then generated, even in dilute suspensions without interparticle interactions. The mean value of T in the solitary swimming, $T_{mean}^{sol} = \int (T dA)/A$, is shown in figure 13(a), where A is the membrane surface area of the swimmer. Here $T_{mean}^{sol}/\mu U_0$ increased according to Ca . The tension of pushers was always higher than that of pullers because pusher swimmers displayed a dented shape in the back (cf. figure 1), and tended to have a higher T_{mean}^{sol} compared with other swimmer types.

Considering variation in the tension due to the hydrodynamic interactions within the suspension, the averaged incremental tension from the solitary swimming $\langle T_{mean} \rangle_{N,t}/T_{mean}^{sol}$ was lower for pushers (cf. figure 13b) because they are more likely to pass each other. As shown in figure 13(c), the slip-through effect of pushers was effective even at higher number densities; among the pullers, tension increased according to number density. Regarding pullers, tensions were strongly influenced by Ca . When $Ca = 0.03$, $\langle T_{mean} \rangle_{N,t}/T_{mean}^{sol}$ was approximately 3.2, and the value monotonically decreased according to Ca .

The instantaneous maximum tension in the suspension was determined; the time averages are shown in figure 13. Both swimmers showed similar trends in Ca and ϕ . As Ca increased with fixed ϕ , the maximum tension slightly decreased. Softer swimmers were able to avoid hard collisions, potentially explaining why the maximum tension was reduced by Ca , whereas the maximum tension linearly increased according to ϕ . The frequency of many-body interferences increased according to number density. Accordingly, the capsular membrane experienced greater tension.

The tension distribution changed with pushing and pulling hydrodynamic interactions. The incremental tension during the short-range interaction was evaluated as a function

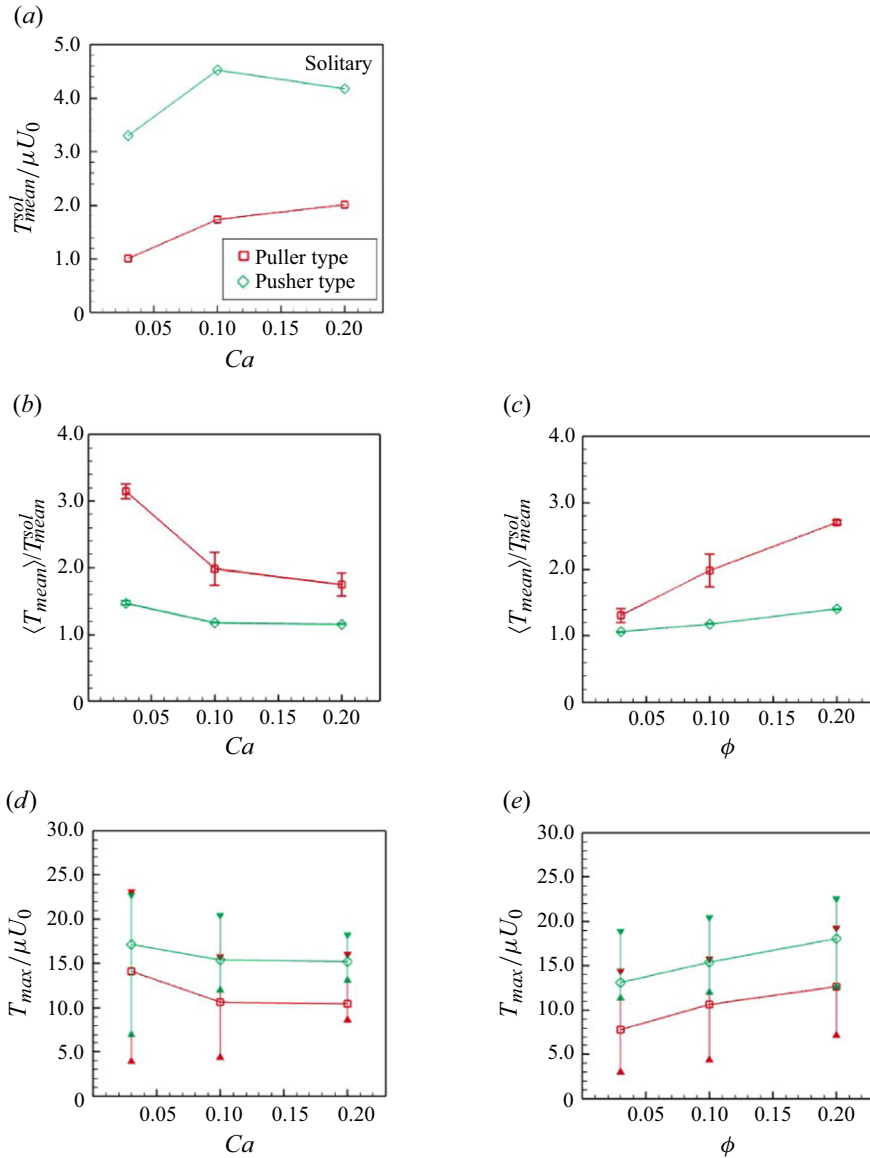


Figure 13. In-plane isotropic tension of swimmers $T(= (\tau_1 + \tau_2)/2)$. Tensions are derived in each triangular element and then averaged over swimmers and times. (a) Mean tension of the solitary swimming. (b,c) Mean tension normalised by the solitary swimming. (d,e) Time-averaged maximum tension in the suspension. The bar indicates instantaneous maximum and minimum values of the maximum tension in the suspension.

of the azimuth angle θ relative to the orientation vector, as defined by $\Delta T(\theta)$ in the following:

$$\Delta T(\theta) = \langle T(\theta) - T^{sol}(\theta) \rangle_{N,t}. \quad (4.2)$$

Here $T(\theta)$ is the circumferentially averaged isotropic tension at θ in the suspension and $T^{sol}(\theta)$ is that of solitary swimming. The result is shown in figure 14. In all cases, incremental tension $\Delta T(\theta)$ decreases according to Ca (cf. figures 14a and 14b). Pushers

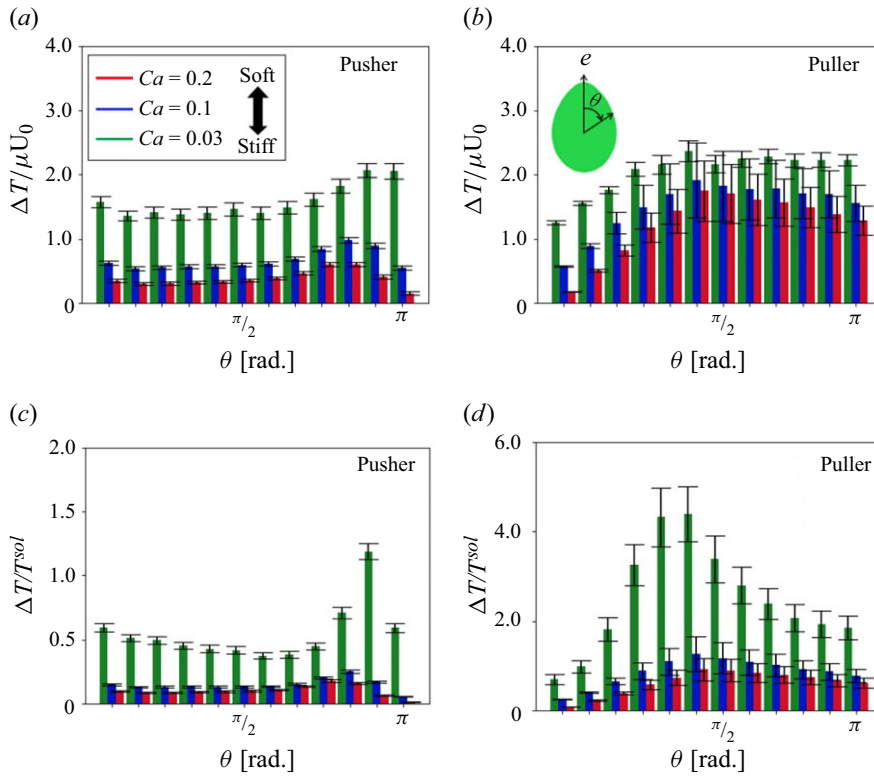


Figure 14. Incremental tension ΔT as a function of the polar angle on a swimmer surface θ ($\phi = 0.1$). (a,b) Distributions of local incremental tension ΔT from the solitary swimming. (c,d) Distributions of the ratio $\Delta T/T_{sol}$.

showed a relatively flat distribution of $\Delta T(\theta)$, except at the $\theta = \pi$ pole, whereas pullers tended to have a decreasing $\Delta T(\theta)$ in the $\theta \leq \pi/2$ region.

Upon further examination of directional distributions that caused the largest tension fluctuations, the incremental tension was normalised according to the value used for solitary swimming. The results are shown in figures 14(c) and 14(d). Among pushers, the ratio of increase was high for $3\pi/4 < \theta < \pi$; among pullers, the ratio of increase was high around $\theta = \pi/2$. These tendencies were more pronounced at low capillary numbers. These results indicate that for pushers (pullers), the greatest change in tension occurs in the posterior (side) during the interaction.

5. Conclusion

In this study we investigated the elastohydrodynamic interactions of deformable soft microswimmers. Membrane deformation altered the mutual interference between swimmers in the cluster, causing closer interactions compared with rigid squirmers. This deformation enables swimmers to more easily slip through each other, weakening the formation of orientation order through short-range interactions. Especially among soft pushers, rotational diffusion due to hydrodynamic interference was reduced, and swimming in the suspension was relatively straight. This ability, induced by membrane deformability, is useful for the propulsion of cells, such as medical microrobots, and it may play an important role in the transport phenomena for high-concentration cell

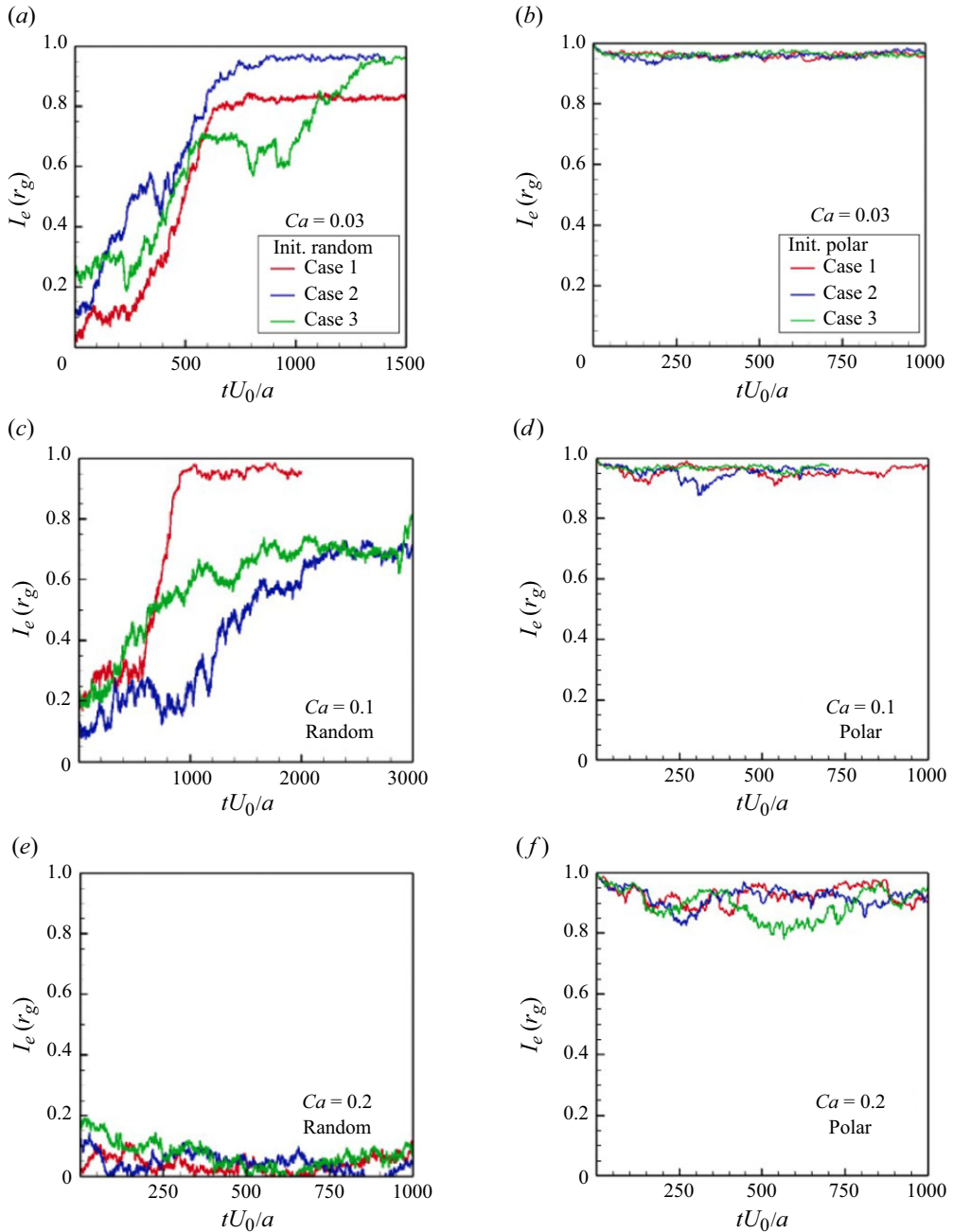


Figure 15. Orientational correlation of the neutral swimmers with $\phi = 0.1$. Each line indicates three different initial conditions with (a,c,e) showing initially random configurations and (b,d,f) initially polar order configurations.

suspensions. On the other hand, pullers showed more proximity interactions with head collisions due to their retraction flow, and an increase in mean membrane tension. However, high deformability led to loosened contacts and smaller increases in tension. These proximity interaction differences resulted in the positional dependence of the

tension in each swimmer mode. For pushers (pullers), the rear (side) interaction produced the greatest change in tension. These findings based on membrane dynamics is expected to contribute to a better understanding of microbial physiological reactions via their mechanotransduction, and to the control of membrane deformation and rupture in medical microrobots for drug delivery. In conclusion, membrane deformability can significantly alter the short-range interactions of the swimmers, such that pushers gain straightness in their trajectories and pullers generate high membrane tension.

Funding. K.K. was supported by Japan Science and Technology Agency SPRING (no. JPMJSP2114). T.I. was supported by the Japan Society for the Promotion of Science Grant-in-Aid for Scientific Research (JSPS KAKENHI grant no. 21H04999 and no. 21H05308). T.O. was supported by Japan Science and Technology Agency PRESTO (no. J210002385) and the Japan Society for the Promotion of Science Grant-in-Aid for Scientific Research (JSPS KAKENHI grant no. 24H01458).

Declaration of interests. The authors report no conflict of interest.

Appendix. Microstructure of soft neutral swimmers

In this appendix we discuss the global order correlation I_e for soft neutral swimmers. A characteristic property of neutral swimmers is the emergence of a coherent polar order, as shown in [figure 15\(a–d\)](#). Polar structures are well developed, especially in low Ca , and they are asymptotic to the rigid squirmers (Yoshinaga and Liverpool, 2008). As Ca increases, the time to the order alignment increases, such that it is approximately $tU_0/a > 600$ for $Ca = 0.03$ and $tU_0/a > 1000$ for $Ca = 0.1$. The development of polar order was not observed at $Ca = 0.2$; however, the structure was maintained for a long duration when the initial conditions were polar. These results indicate that membrane deformation for neutral swimmers changes their short-range interactions with respect to the orientational alignments after the interference. Thus, the time scale concerning the appearance of the collective swimming tends to be slower for soft neutral swimmers than that for stiff swimmers.

REFERENCES

- BARTHÈS-BIESEL, D., DIAZ, A. & DHENIN, E. 2002 Effect of constitutive laws for two-dimensional membranes on flow-induced capsule deformation. *J. Fluid Mech.* **460**, 211–222.
- BATCHELOR, G.K. 1970 The stress system in a suspension of force-free particles. *J. Fluid Mech.* **41** (3), 545–570.
- BATCHELOR, G.K. & GREEN, J.T. 1972 The determination of the bulk stress in a suspension of spherical particles to order c^2 . *J. Fluid Mech.* **56**, 401–427.
- BEENAKKER, C.W.J. 1986 Ewald sum of the Rotne–Prager tensor. *J. Chem. Phys.* **85** (3), 1581–1582.
- BLAKE, J.R. 1971 A spherical envelope approach to ciliary propulsion. *J. Fluid Mech.* **46** (1), 199–208.
- BLANC, F., LEMAIRE, E., MEUNIER, A. & PETERS, F. 2013 Microstructure in sheared non-Brownian concentrated suspensions. *J. Rheol.* **57** (1), 273–292.
- BOSSIS, G. & BRADY, J.F. 1987 Self-diffusion of Brownian particles in concentrated suspensions under shear. *J. Chem. Phys.* **87** (9), 5437–5438.
- BRADY, J.F. & BOSSIS, G. 1985 The rheology of concentrated suspensions of spheres in simple shear flow by numerical simulation. *J. Fluid Mech.* **155**, 105–129.
- BRADY, J.F. & BOSSIS, G. 1988 Stokesian dynamics. *Annu. Rev. Fluid Mech.* **20** (1), 111–157.
- BRENNER, H. 1974 Rheology of a dilute suspension of axisymmetric Brownian particles. *Intl J. Multiphase Flow* **1** (2), 195–341.
- COBURN, L., CERONE, L., TORNEY, C., COUZIN, I.D. & NEUFELD, Z. 2013 Tactile interactions lead to coherent motion and enhanced chemotaxis of migrating cells. *Phys. Biol.* **10** (4), 046002.
- DAVIS, R.H. & ACRIVOS, A. 1985 Sedimentation of noncolloidal particles at low Reynolds numbers. *Annu. Rev. Fluid Mech.* **17** (1), 91–118.
- EINSTEIN, A. 1906 Eine neue Bestimmung der Moleküldimensionen. *Ann. Phys.* **324** (2), 289–306.
- GUAZZELLI, É. & POULIQUEN, O. 2018 Rheology of dense granular suspensions. *J. Fluid Mech.* **892**, P1.

- HELFRICH, W. 1973 Elastic properties of lipid bilayers: theory and possible experiments. *Z. Naturforsch. C* **28** (11–12), 693–703.
- ISHIKAWA, T. 2024 Fluid dynamics of squirmers and ciliated microorganisms. *Annu. Rev. Fluid Mech.* **56** (1), 119–145.
- ISHIKAWA, T., DANG, T.N. & LAUGA, E. 2022 Instability of an active fluid jet. *Phys. Rev. Fluids* **7** (9), 013104.
- ISHIKAWA, T. & KIKUCHI, K. 2018 Biomechanics of *Tetrahymena* escaping from a dead end. *Proc. R. Soc. Lond. B* **285** (1873), 20172368472.
- ISHIKAWA, T., LOCSEI, J.T. & PEDLEY, T.J. 2008 Development of coherent structures in concentrated suspensions of swimming model micro-organisms. *J. Fluid Mech.* **615**, 401–431.
- ISHIKAWA, T. & PEDLEY, T.J. 2007 Diffusion of swimming model micro-organisms in a semi-dilute suspension. *J. Fluid Mech.* **588**, 437–462.
- ISHIKAWA, T. & PEDLEY, T.J. 2008 Coherent structures in monolayers of swimming particles. *Phys. Rev. Lett.* **100** (8), 088103.
- ISHIKAWA, T., SIMMONDS, P.M. & PEDLEY, T.J. 2006 Hydrodynamic interaction of two swimming model micro-organisms. *J. Fluid Mech.* **568**, 119–160.
- ISHIKAWA, T., TANAKA, T., IMAI, Y., OMORI, T. & MATSUNAGA, D. 2016 Deformation of a micro-torque swimmer. *Proc. R. Soc. Lond. A* **472** (2185), 20150604.
- JEFFERY, D.J. & ACRIVOS, A. 1976 The rheological properties of suspensions of rigid particles. *AIChE J.* **22** (3), 417–432.
- JENNINGS, H.S. 1904 The behavior of Paramecium. Additional features and general relations. *J. Comp. Neurol. Psychol.* **14** (6), 441–510.
- KATOH, T.A., *et al.* 2023 Immotile cilia mechanically sense the direction of fluid flow for left-right determination. *Science* **379** (6627), 66–71.
- KRIEGER, I.M. & DOUGHERTY, T.J. 1959 A mechanism for non-Newtonian flow in suspensions of rigid spheres. *Trans. Soc. Rheol.* **3** (1), 137–148.
- KYOYA, K., MATUNAGA, D., OMORI, T. & ISHIKAWA, T. 2015 Shape matters: near-field fluid mechanics dominate the collective motions of ellipsoidal squirmers. *Phys. Rev. E* **92** (6), 063027.
- LAC, E., BARTHES-BIESEL, D., PELEKASIS, N.A. & TSAMOPOULOS, J. 2004 Spherical capsules in three-dimensional unbounded Stokes flows: effect of the membrane constitutive law and onset of buckling. *J. Fluid Mech.* **516**, 303–334.
- LAC, E., MOREL, A. & BARTHES-BIESEL, D. 2007 Hydrodynamic interaction between two identical capsules in simple shear flow. *J. Fluid Mech.* **573**, 149–169.
- LIGHTHILL, M.J. 1952 On the squirming motion of nearly spherical deformable bodies through liquids at very small Reynolds numbers. *Commun. Pure Appl. Maths* **5** (2), 109–118.
- LÖBER, J., ZIEBERT, F. & ARANSON, I.S. 2015 Collisions of deformable cells lead to collective migration. *Sci. Rep.* **5** (1), 9172.
- LOEWENBERG, M. & HINCH, E.J. 1997 Collision of two deformable drops in shear flow. *J. Fluid Mech.* **338**, 289–315.
- MARI, R., SETO, R., MORRIS, J.F. & DENN, M.M. 2014 Shear thickening, frictionless and frictional rheologies in non-Brownian suspensions. *J. Rheol.* **58** (6), 1693–1724.
- MATSUI, H., OMORI, T. & ISHIKAWA, T. 2020a Hydrodynamic interaction of two deformable torque swimmers. *J. Fluid Mech.* **894**, A9.
- MATSUI, H., OMORI, T. & ISHIKAWA, T. 2020b Rheology of a dilute suspension of deformable microswimmers. *Phys. Fluids* **32** (7), 071902.
- MENZEL, A.M. & OHTA, T. 2012 Soft deformable self-propelled particles. *EPL* **99** (5), 58001.
- NESS, C., SETO, R. & MARI, R. 2022 The physics of dense suspensions. *Annu. Rev. Condens. Matter Phys.* **13** (1), 97–117.
- OMORI, T., ISHIKAWA, T., BARTHÈS-BIESEL, D., SALSAC, A.-V., IMAI, Y. & YAMAGUCHI, T. 2012 Tension of red blood cell membrane in simple shear flow. *Phys. Rev. E* **86** (5), 056321.
- OMORI, T., ISHIKAWA, T., IMAI, Y. & YAMAGUCHI, T. 2013 Shear-induced diffusion of red blood cells in a semi-dilute suspension. *J. Fluid Mech.* **724**, 154–174.
- PEROZO, E., CORTES, D.M., SOMPORNISUT, P., KLODA, A. & MARTINAC, B. 2002 Open channel structure of MscL and the gating mechanism of mechanosensitive channels. *Nature* **418** (6901), 942–948.
- POZRIKIDIS, C. 1992 Generalized boundary integral methods. In *Boundary Integral and Singularity Methods for Linearized Viscous Flow*, chap. 4, pp. 103–138. Cambridge University Press.
- POZRIKIDIS, C. 2010 *Computational Hydrodynamics of Capsules and Biological Cells*, chap. 2. CRC.
- RUSSEL, W.B. 1980 Review of the role of collidal forces in the rheology of suspension. *J. Rheol.* **24** (3), 287–317.
- SAINTILLAN, D. 2018 Rheology of active fluids. *Annu. Rev. Fluid Mech.* **50** (1), 563–592.

- SKALAK, R., TOZEREN, A., ZARADA, R.P. & CHIEN, S. 1973 Strain energy function of red blood cell membranes. *Biophys. J.* **13**, 245–264.
- SUKHAREV, S.I., BLOUNT, P., MARTINAC, B. & KUNG, C. 1997 Mechanosensitive channels of *Escherichia coli*: the MscL gene, protein, and activities. *Annu. Rev. Physiol.* **59** (1), 633–657.
- WALTER, J. , SALSAC, A.-V., BARTHES-BIESEL, D. & TALLEC, P.L. 2010 Coupling of finite element and boundary integral methods for a capsule in a Stokes flow. *Intl J. Numer. Meth. Engng* **83** (7), 829–850.
- WALTER, J. , SALSAC, A.-V. & BARTHES-BIESEL, D. 2011 Ellipsoidal capsules in simple shear flow: prolate versus oblate initial shapes. *J. Fluid Mech.* **676**, 318–347.
- WEN, H., ZHU, Y., PENG, C., KUMAR, P.B.S. & LARADJI, M. 2022 Collective motion of cells modeled as ring polymers. *Soft Matt.* **18** (6), 1228–1238.
- YOSHINAGA, N. & LIVERPOOL, T.B. 2008 From hydrodynamic lubrication to many-body interactions in dense suspensions of active swimmers. *Eur. Phys. J. E* **41**, 76.
- ZÖTTL, A. & STARK, H. 2016 Emergent behavior in active colloids. *J. Phys.: Condens. Matter* **28**, 253001.